The Solidification and Welding Metallurgy of Galling-Resistant Stainless Steels

The autogenous welding response of common galling-resistant stainless steels are evaluated and compared

BY C. V. ROBINO, J. R. MICHAEL AND M. C. MAGUIRE

ABSTRACT. The autogenous welding behavior of two commercial galling-resistant austenitic stainless steels, Nitronic 60 and Gall-Tough, was evaluated and compared. The solidification behavior and fusion zone hot-cracking tendency of the alloys was evaluated by using differential thermal analysis, Varestraint testing and laser spot-welding trials. Gleeble thermal cycle simulations were used to assess the hot ductility of the alloys during both on-heating and on-cooling portions of weld thermal cycles. Solidification microstructures were characterized by light optical and electron microscopy, and the solidification modes and phases were identified. Gas tungsten arc (GTA) welds in both alloys solidified by the ferritic-austenitic mode, and their behavior was best described using chromium and nickel equivalents developed specifically for the Nitronic series of alloys. Both alloys were found to be somewhat more susceptible to solidification hot cracking than conventional austenitic stainless steels, although the cracking resistance of Nitronic 60 was somewhat superior to Gall-Tough. Laser spot-welding trials resulted in both fusion and heat-affected zone cracking in the Nitronic 60, while Gall-Tough was resistant to cracking in these high-solidification-rate welds. Comparison of the laser weld microstructures indicated that Nitronic 60 shifts to fully austenitic solidification, while Gall-Tough shifts to an austenitic-ferritic solidification mode in high-energy-density processing. The hot ductility measurements indicated that Gall-Tough is generally superior to Nitronic 60 in both on-heating and on-cooling tests, apparently as a result of differences in grain size and the mechanism of ferrite formation at high temperatures.

C. V. ROBINO, J. R. MICHAEL and M. C. MAGUIRE are with Sandia National Laboratories, Albuquerque, N.Mex.

Introduction

Conventional austenitic stainless steels typically display relatively poor galling resistance in many applications, and, as a result, a variety of nonstandard austenitic steels have been developed to overcome this difficulty. These steels are normally high-silicon, high-manganese, nitrogen-strengthened alloys and include such grades as Nitronic 60, Gall-Tough and Gall-Tough PLUS. Fusion welding of these alloys by conventional filler metal processes such as shielded metal arc (SMA) and cold wire feed gas tungsten arc (GTA) welding is normally not problematic (Ref. 1). For these processes, standard filler metals (*e.g.*, E/ER 240 and E/ER 308) and specially developed fillers (*e.g.*, ER 218) generally provide satisfactory welding response and weldment performance; however, in situations requiring autogenous and/or high-energy density (HED) processing, the solidification behavior and cracking tendency of the alloys is important.

The autogenous weldability of this class of alloys has not been reported in the literature, although the general welding behavior of Nitronic 60 was evaluated by Espy (Ref. 1). In that work, Espy developed a modified Schaeffler diagram to describe the ferrite content of welds in the Nitronic series of alloys. In addition, mechanical properties for these alloys and case studies of welded fabrication were discussed. Maguire, *et al.* (Ref. 2), examined the heat-affected zone (HAZ) cracking behavior of Nitronic 60 using gas tungsten arc welding (GTAW) and HED processing, as well as weld thermal cycle simulations. Depending on the GTAW conditions, both HAZ liquation and subsolidus cracking were observed. For HED overlapping spot welds, HAZ cracking was observed under essentially all processing conditions.

KEY WORDS

Galling Resistant
GTAW
Hot Ductility
LBW
Solidification
Stainless Steels
Varestraint Testing
Weldability

There have been a number of investigations of the weld solidification behavior, solidification mode and weld cracking behavior of nitrogen-alloyed and high-manganese, nitrogen-strengthened stainless steels (Refs. 3–7). In addition, there have been several comprehensive reviews detailing the many aspects pertaining to the welding of austenitic stainless steels (Refs. 8, 9). In general , the results of these works indicate that the effects of manganese and nitrogen can be rationalized with current austenitic stainless steel theory, although the roles of these elements are relatively complex (Ref. 5).

In the case of the three alloys mentioned above, the alloy design approach appears to be similar, although there are some differences in the balance of alloy additions. These differences are most distinct between Nitronic 60 and Gall-Tough, while the Gall-Tough PLUS alloy is generally similar in composition to Nitronic 60. The Gall-Tough alloy is balanced to a somewhat higher Cr_{eq}/Ni_{eq} ratio than Nitronic 60, which implies that higher as-solidified ferrite contents are likely and that the autogenous weldability of the two alloys may be different. Therefore, the purpose of the present study was to evaluate and compare the solidification and autogenous weldability of Nitronic 60 and Gall-Tough alloys. Fusion, HAZ behavior and laser weldability were examined and evaluated.

Experimental Procedure

The alloys used in this study were from commercial heats of Nitronic 60 and Gall-Tough, and the compositions of the heats are shown in Table 1. From these heats, samples for differential thermal analysis, hot ductility testing, and Varestraint testing were machined. All heats were tested in the mill-annealed condition. Table 1 also shows the compositions of the 304L and 316 stainless steels used for comparison of hot-cracking response.

Differential thermal analysis (DTA) experiments were performed using a Netsch STA 429 thermal analyzer on samples of approximately 750 mg mass. Tungsten (>99.99% purity) was used as the reference material. Both the reference and the samples were held in high purity alumina crucibles during testing. All tests were run in a flowing-helium atmosphere at heating and cooling rates of 0.33°C/s (0.59°F/s). The peak temperature during testing was approximately 1500°C (2732°F). Previous experience (Ref. 10) with this equipment and procedures indicated that a reproducibility of approximately 2°C (3.6°F) in measured temperatures could be expected. Interpretation of the DTA curves was conducted using the convention established by MacIssac, *et al.* (Ref. 11).

Susceptibility to fusion-zone hot cracking was quantified using the longitudinal Varestraint test (Ref. 12). Varestraint samples measuring 165 × 25 × 3 mm were fabricated with the long dimension parallel to the plate rolling direction. Autogenous GTAW was used in the tests. The welding parameters were 100 A direct current electrode negative, 12.5 V and 3.6 mm/s travel speed. Argon was used as the shielding gas (20 L/min flow rate) and electrodes were constructed of ceriated tungsten. Two samples were tested at each augmented strain over the range from 0.25 to 3.5%. Cracks in the fusion zone were measured by using an optical measuring microscope with fluorescent illumination. The primary measures of cracking susceptibility were taken as the maximum crack length (MCL) and total crack length (TCL) on each sample.

Laser welding trials were conducted with a Raytheon 55501 400-W average power pulsed Nd:YAG laser. Laser spot welds were produced at sharp focus with a 10-J, 7.2-ms pulse. Laser welds were produced using the same laser parameters operating at a pulse frequency of 8 Hz and travel speed of 1.6 mm/s.

The susceptibility of the alloys to HAZ cracking was assessed by hot ductility testing performed on a Gleeble 1500 thermomechanical simulator. This test subjects the alloy to a simulated HAZ thermal cycle, which is interrupted by rapid fracture during either the on-heating or on-cooling portion of the thermal cycle. The thermal cycle used was determined from the Gleeble software and represents a cycle very close to the fusion boundary of a 3.94 kJ/mm weld in a 12.7-mm-thick plate. The peak temperature for these tests was approximately 15°C (27°F) below the nil-strength temperature (NST), although the effect of peak temperature was also evaluated in several cases. The NST was determined by imposing a tensile load of approximately 175 N on a hot ductility sample and ramping up the temperature at 100°C/s (180°F/s) until sample failure. The hot ductility samples were 6.35-mm-diameter rods. During hot ductility testing, the samples were loaded at a crosshead velocity of 2 cm/s and ductility was measured as the reduction of area at the fracture surface.

As-received material, DTA samples and welds were examined by light optical metallography. Sample preparation for the microstructural examinations included mounting and polishing through 0.05-μm colloidal silica using standard metallographic procedures. Samples were electrolytically etched using a 10% oxalic acid solution at room temperature and 6 V. Ferrite fraction measurements were conducted using a calibrated magnegage. Analytical electron microscopy (AEM) was used for further characterization of selected samples. For these analyses, thin foil specimens were prepared by electrolytic thinning in a 10% HNO_3 in methanol solution at –40°C (–40°F) and 15 VDC. A Phillips EM30 AEM, operating at an accelerating potential of 300 kV and equipped with an Oxford Instruments energy dispersive spectrometer (EDS), was used for foil analysis. Scanning electron microscopy (SEM) was also used on selected samples. In this case, samples were polished (or polished and etched) sections and were generally examined in the backscattered electron or secondary electron imaging modes, respectively, in a JEOL 6400 or Hitachi 54500 SEM operating at 20 kV. Identification of microstructural constituents was conducted by combinations of AEM, electron microprobe analysis (EPMA) and through the use of backscattered electron Kikuchi patterns (BEKP) in the SEM (Ref. 13).

Electron probe microanalysis was performed on a JEOL 8600 electron microprobe X-ray analyzer operating at 15 kV, a spot size of approximately 1 μm and beam current of 25 nA. Elemental composition data was determined by established $\phi(pz)$ algorithms with integrated K_α X-ray intensities (Ref. 14). BEKP analysis was conducted on a JEOL 6400 SEM equipped with a custom-made charge coupled device (CCD) based detector for BEKP (Ref. 13). Patterns were collected at an accelerating voltage of 20 kV and a beam current of 1 nA and were obtained by stopping the beam on a feature of interest and collecting a BEKP by exposing the CCD camera for 10–20 s. Phase identification was accomplished by automatic extraction of the important crystallographic information from the patterns. The crystallographic parameters are then used in conjunction with qualitative chemical information determined by EDS analysis to search a crystallographic database. Once a candidate match is obtained, the patterns are simulated and the simulation is compared with the original pattern.

Results and Discussion

GTA Weld Solidification Mode and Ferrite Content

Figure 1A, B shows the microstructures and BEKP analysis of the various

Table 1 — Alloy Compositions

Element	Nitronic 60 (Gleeble)	Nitronic 60 (Varestraint)	Gall-Tough	304L	316
Ni	8.88	8.31	5.17	9.20	10.10
Cr	16.75	16.45	16.23	18.31	16.30
Mn	8.46	8.36	5.50	1.42	1.22
Si	3.96	3.91	3.48	0.64	0.42
Mo	0.38	—	—	0.25	2.05
Cu	—	—	—	0.46	0.24
Co	—	—	—	0.11	0.23
C	0.078	0.071	0.10	0.021	0.043
N	0.15	0.15	0.15	0.080	0.051
P	0.027	0.029	0.023	0.025	0.031
S	0.005	0.012	0.020	0.018	0.010
Fe	bal.	bal.	bal.	bal.	bal.

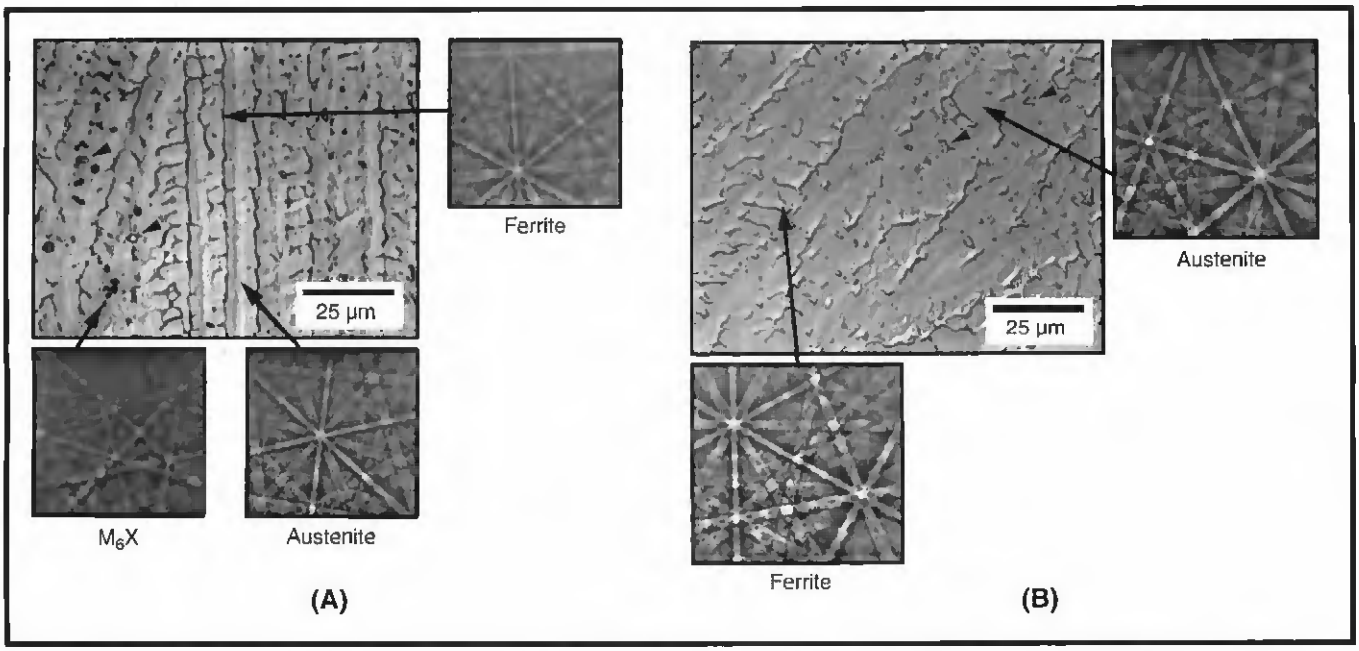

Fig. 1 — Microstructures of GTA welds in Nitronic 60 and Gall-Tough. A — Nitronic 60, ferrite number 3.9; B — Gall-Tough, ferrite number 11.4. Small arrowheads indicate location of eutectic ferrite.

constituents in autogenous GTA welds in Nitronic 60 and Gall-Tough, respectively. Both welds were found to solidify in the ferritic-austenitic mode, although the quantity of room-temperature ferrite differed for the two alloys. For the Nitronic 60 the average ferrite content of the welds was 3.9 FN, while the average for the Gall-Tough welds was 11.4 FN. In the ferritic-austenitic solidification mode (Refs. 3, 4, 8, 9, 15), the primary solidification phase is ferrite, while austenite forms in the terminal stage of solidification by a liquid/ferrite/austenite reaction. The primary δ-ferrite then transforms to austenite by a diffusional mechanism. Delta ferrite, which is retained at room temperature, is thereby located at the cores of the original dendrites. Following Brooks and Thompson (Ref. 9), retained ferrite formed by this mechanism is referred to as "skeletal ferrite" in the current work. In addition to the skeletal ferrite, both alloys also appeared to contain a small fraction of eutectic ferrite. As has been discussed by others (Refs. 6, 15, 16), welds that solidify in the ferritic-austenitic solidification mode may contain some eutectic ferrite in addition to the primary δ-ferrite. This eutectic ferrite can be distinguished (Ref. 7) from the primary δ-ferrite by a variety of features, including location in the microstructure, morphology, solute distribution in the austenite adjacent to the ferrite, solute distribution in the ferrite itself, average ferrite composition and the amount of interfacial precipitation. Eutectic ferrite was also observed by Ritter, *et al.* (Ref. 6), in a niobium-modified Nitronic 50-W weld filler metal that solidified in the ferritic-austenitic mode. In the present study, the eutectic ferrite was identified by BEKP analysis, shape and location in the microstructure and by its tendency to be associated with other minor constituents, such as carbides in the case of Nitronic 60 — Fig. 1A. The BEKPs obtained for the various constituents are also shown. For both the Nitronic 60 and Gall-Tough alloys, the eutectic ferrite is not a predominant feature of the microstructure, although as discussed by Ritter, *et al.* (Ref. 6), its presence does indicate that the composition of the alloy must be close to the eutectic trough.

The retained ferrite content of the base metals and GTA welds are compared in Table 2. As shown, the wrought Nitronic 60 alloy is fully austenitic, while the Gall-Tough alloy contains a small fraction of retained ferrite in this condition. For the GTA welds, the heat of Nitronic 60 evaluated in this work has a ferrite fraction close to the lower limit considered acceptable for avoiding hot cracking. Conversely, the Gall-Tough heat is close to the upper limit of the ferrite range usually specified to minimize solidification hot cracking. In any case, it is clear that the ferrite-forming potential of the two alloys is significantly different.

It is notable to compare the ferrite content of the GTA welds with that predicted by the various ferrite fraction diagrams available in the literature. Considering

Table 2 — Results of Ferrite Measurements

Condition	Alloy	Average FN
Base Metal	Nitronic 60	0
	Gall-Tough	1.5
GTA Weld	Nitronic 60	3.9
	Gall-Tough	11.4

first the Welding Research Council (WRC) 1992 diagram (Ref. 8) shown in Fig. 2, it is apparent that this diagram does not adequately predict either the solidification mode or ferrite fraction for either alloy. The WRC 1992 diagram is generally considered applicable for manganese contents up to 10 wt-% (even though it is not included in the equivalents used), molybdenum contents up to 3 wt-%, nitrogen contents up to 0.2 wt-% and silicon contents up to 1 wt-%. Of these elements, the silicon content of the present alloys at 3.5– 4.0 wt-% is significantly out of this range; therefore, it seems likely that it is a major factor affecting the accuracy of the diagram for these types of alloys. Elemental segregation patterns determined by EPMA were essentially similar to those observed by Suutala, *et al.* (Ref. 15), for alloys solidifying in the ferritic-austenitic mode. Silicon generally segregated in a manner similar to that for chromium and was consequently enriched (to levels approaching 5 wt-%) in the skeletal ferrite.

The effects of manganese and nitrogen on the solidification mode and ferrite content of austenitic stainless steels

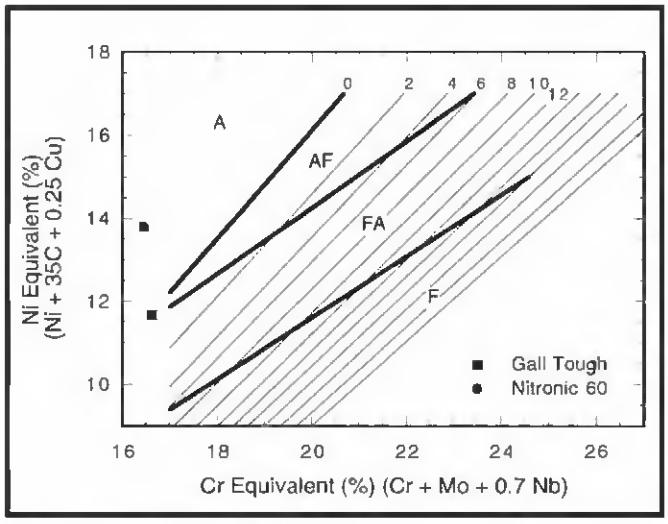

Fig. 2 — WRC 1992 diagram showing compositions of Nitronic 60 and Gall-Tough.

are also complicated. Suutala (Ref. 5) conducted a comprehensive evaluation of many GTA welds and considered the applicability of the various (Ref. 8) chromium and nickel equivalents, Cr_{eq} and Ni_{eq}, respectively, for prediction of solidification mode and ferrite content. For manganese contents 5 – 8 wt-%, Suutala (Ref. 5) found that the equivalents developed by Hull (Ref. 17) gave the most satisfactory correlation between composition and solidification mode or ferrite content (if consistency with other austenitic stainless steels is to be maintained). The equivalents developed by Hull are given by

$$Cr_{eq}\text{ (Hull)} = Cr + 1.21(Mo) + 0.48(Si) + 0.14(Nb) + 2.20(Ti) \quad (1)$$

$$Ni_{eq}\text{ (Hull)} = Ni + 0.11(Mn) - 0.0086(Mn)^2 + 24.6(C) + 18.4(N) + 0.44(Cu) \quad (2)$$

where elemental fractions are given in wt-%. Figure 3 shows the solidification mode and ferrite content estimates for Nitronic 60 and Gall-Tough using the data and correlations of Suutala (Ref. 5) and Hull (Ref. 17). The predictions for so-

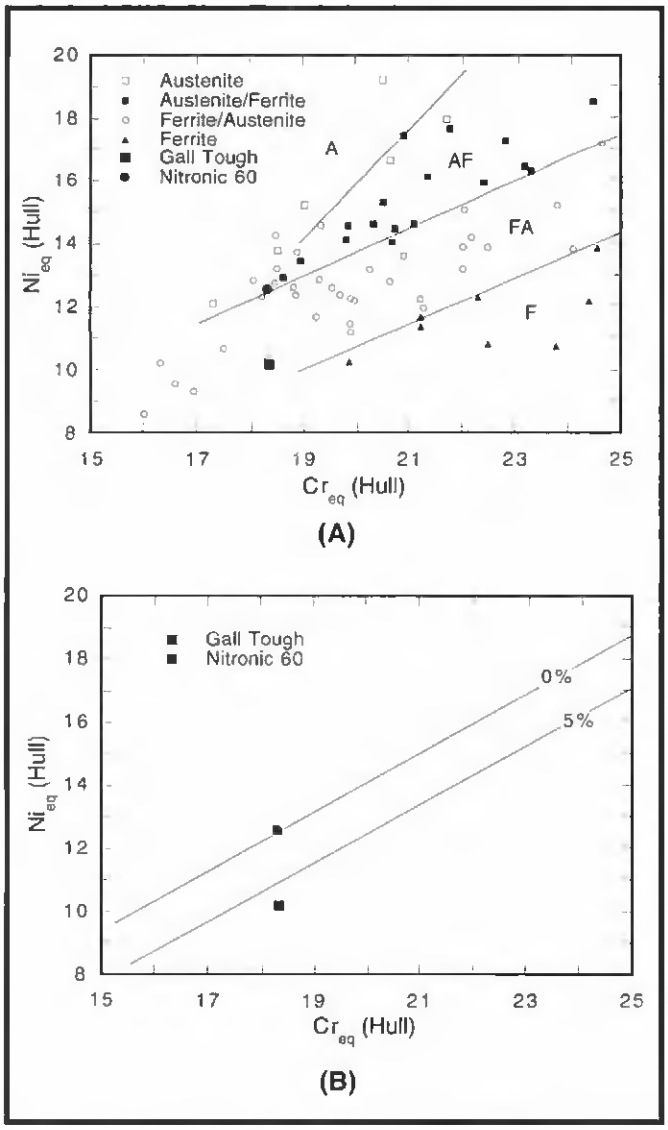

Fig. 3 — Diagrams constructed using Hull chromium and nickel equivalents. A — Solidification mode; B — ferrite content.

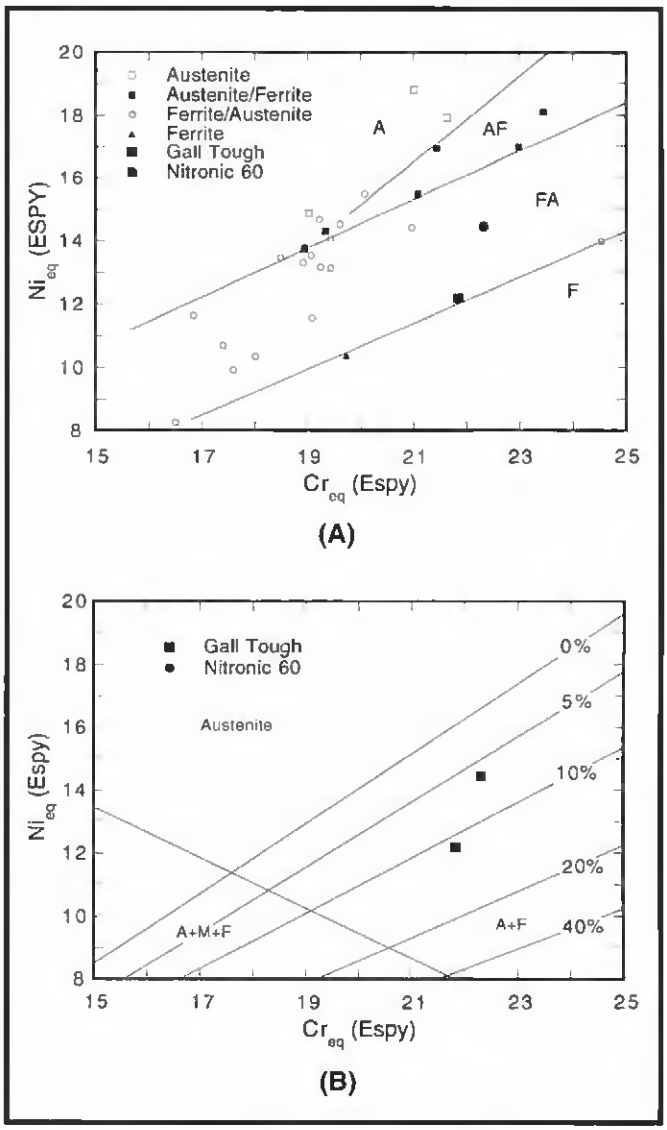

Fig. 4 — Diagrams constructed using Espy chromium and nickel equivalents. A — Solidification mode; B — ferrite content.

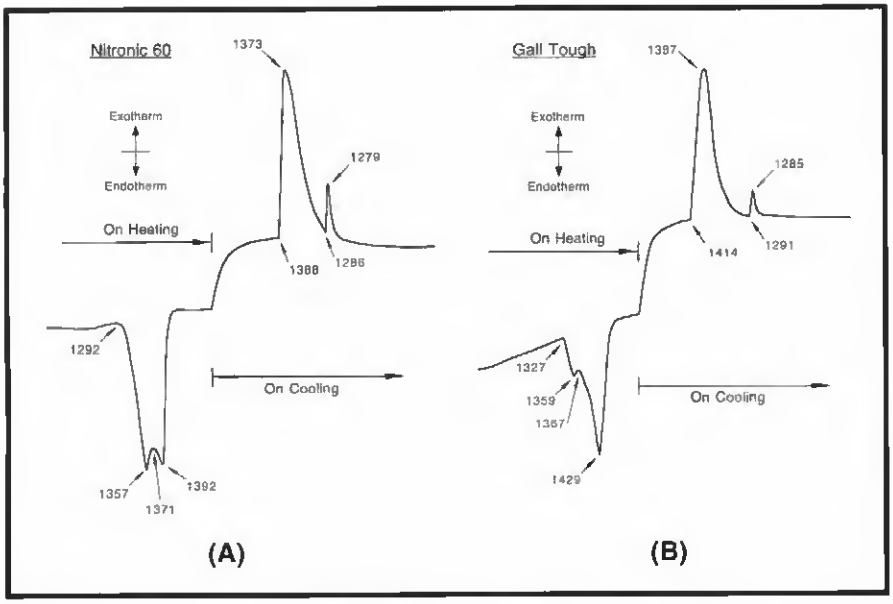

Fig. 5 — DTA thermograms. A — Nitronic 60; B — Gall-Tough for heating and cooling rates of 0.33°C/s (32.6°F/s). Labeled deviations from local baseline are given in centigrade.

lidification mode as shown in Fig. 3A are essentially correct for both alloys, although the estimate for Nitronic 60 is somewhat ambiguous. In terms of ferrite content, the Hull equivalents underestimate the measured value by approximately 4 FN, assuming that FN is approximately equal to volume percent, as is normally the case below about 8 FN (Ref. 8). The correlation seems satisfactory given the typical accuracy of ferrite number predictions and the uncertainty in ferrite number measurements (Brooks and Lippold [Ref. 8] note that variation between predicted and measured values commonly differ by as much as 4–8 FN). It is also important to note that of the various equivalent formulations evaluated by Suutala (Ref. 5), those shown in Fig. 3 provide the best representation of the Nitronic 60 and Gall-Tough results. However, these correlations consider a wide range of alloy types and are not optimized with respect to the unique compositions of the anti-galling steels.

Modifications of the original Schaeffler (Ref. 18) equivalents, which are specific to the anti-galling alloys, were developed by Espy (Ref. 1) to describe the Nitronic series of alloys. These equivalents have the form

$$C_{req}\,(\text{Espy}) = \text{Cr} + \text{Mo} + 1.5(\text{Si}) + 0.5(\text{Nb}) + 5(\text{V}) + 3(\text{Al}) \quad (3)$$

$$Ni_{eq}\,(\text{Espy}) = \text{Ni} + 30(\text{C}) + 0.87\,(\text{for Mn}) + 0.33(\text{Cu}) + 30(\text{N} - 0.04\text{S}) \quad (4)$$

Espy (Ref. 1) did not construct a solidification mode diagram for these steels. Such a diagram was constructed by Ritter and Savage (Ref. 6) who replotted the data of Suutala (Ref. 5) for compositions high in manganese and nitrogen using Espy's equivalents. Figure 4 shows solidification mode and ferrite content diagrams from the work of Ritter and Savage and Espy, respectively, and includes the current alloy compositions. Agreement between the observed and predicted solidification mode and ferrite content is quite good. Since these diagrams were developed

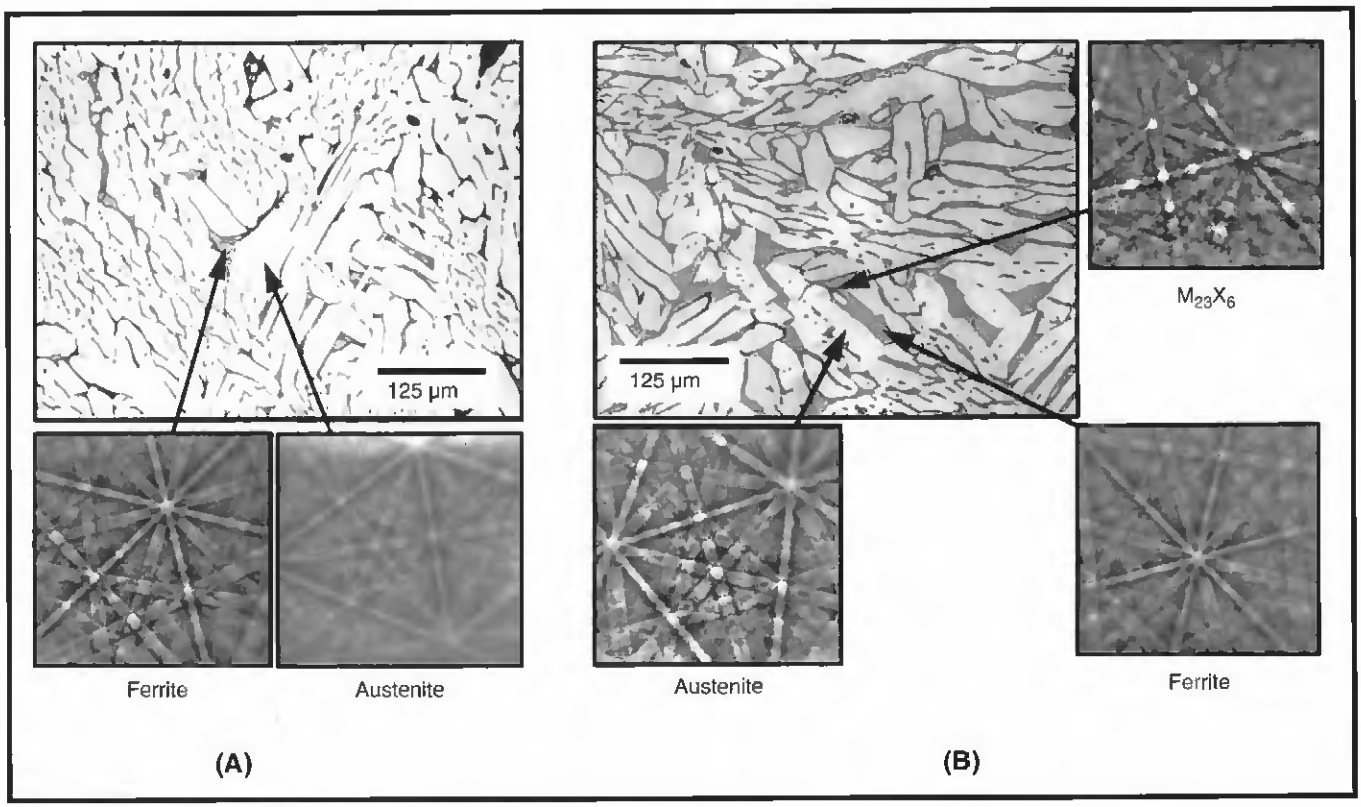

Fig. 6 — Microstructures of DTA samples. A — Nitronic 60; B — Gall-Tough (small arrowheads indicate location of eutectic ferrite).

specifically for nitrogen-strengthened, high-manganese steels, it is not surprising they provide the best description of solidification mode and ferrite content of Nitronic 60 and Gall-Tough alloys. Nevertheless, it seems appropriate that the diagrams in Fig. 4 are preferred over the more generalized diagrams shown in Figs. 2 and 3.

Differential Thermal Analysis

Figure 5 compares differential thermal analysis (DTA) traces from the Nitronic 60 and Gall-Tough obtained at heating and cooling rates of 0.33°C/s (0.59°F/s). The temperatures shown on the diagrams are averages from two tests for each alloy, although the temperatures for each run did not differ by more than a few degrees. In general, the melting and solidification behavior of the two alloys is similar, although there are several important quantitative differences. Melting of the Nitronic 60 commences at 1292°C (2358°F), while the Gall-Tough begins to liquate at 1327°C (2421°F). Both alloys display a double-peaked melting endotherm with the initial endotherm being significantly larger in the Nitronic 60. The initial endothermic peak is interpreted as liquation of austenite, although solid-state transformation of austenite to ferrite may also contribute to the endotherm. Ritter, *et al.* (Ref. 7), have examined the high-temperature phase stabilities in Nitronic 50, a similar alloy, and have shown that for heat treatments closer to equilibrium (*i.e.*, long-time isothermal heat treatments) the alloy can be close to 100% δ-ferrite at temperatures near the solidus. Evidence for the solid-state transformation at temperatures below the initial liquation temperature could not be resolved by DTA in either Nitronic 60 or Gall-Tough, but transformation undoubtedly occurs. Further, it is conceivable that the initial endotherm at this heating rate may also reflect continuing solid-state transformation to δ-ferrite, although the major contribution to the peak is from the austenite liquation. Initial austenite liquation/solid-state transformation continues from 1357 to 1359°C (2443 to 2478°F) for the Nitronic 60 and Gall-Tough, respectively. The smaller austenite melting endotherm in the Gall-Tough implies that a greater fraction of austenite in the Gall-Tough undergoes a solid-state transformation to δ-ferrite during heating below the solidus. As melting initiates, the Gall-Tough alloy contains a relatively small fraction of austenite, which appears to be consistent with the higher Cr_{eq}/Ni_{eq} ratio of this alloy. The implications of the differences between Nitronic 60 and Gall-Tough in terms of on-heating transformation and melting behavior are discussed below in detail. Melting of δ-ferrite commences at about 1370°C (2498°F) for both alloys and continues until the liquidus temperature is reached at 1392°C (2538°F) for Nitronic 60 and 1429°C (2604°F) for Gall-Tough. Thermogravimetric analysis during the DTA runs showed little or no (<1 mg) sample weight changes. Thus, it does not appear that there were any significant changes in the sample composition (*e.g.*, volatilization of Mn or N) during the analysis.

Upon cooling from the melt, the Nitronic 60 and Gall-Tough are very similar in their behavior in that the primary solidification event (which generally occurs after some undercooling in the present experiments) is followed by a single terminal solidification reaction. Figure 6 shows the room-temperature microstructures of the DTA samples. As with the GTA welds, solidification initiates with the formation of primary δ-ferrite and the large initial exotherm of the DTA traces corresponds to this reaction. As indicated by the smaller secondary exotherm, both alloys terminate solidification with a (presumably peritectic) reaction between the three phases — liquid, δ-ferrite and austenite. In contrast to the higher-cooling-rate GTA welds, the DTA samples did not contain eutectic ferrite, but, as shown in Fig. 6B, the Gall-Tough alloy did contain an appreciable fraction of $M_{23}X_6$ carbide or nitride precipitates along some of the δ-ferrite-austenite interfaces. These precipitates apparently form as a result of elemental partitioning during the solid-state transformation from δ-ferriteto austenite at temperatures below the solidus.

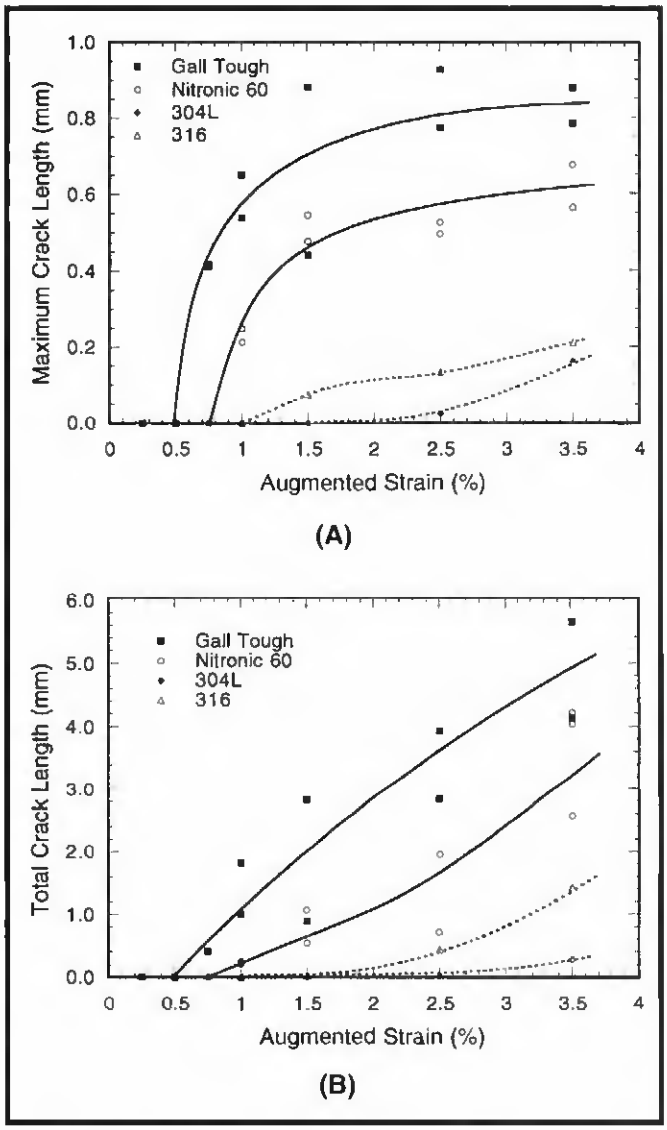

Fig. 7 — Varestraint test results for Nitronic 60, Gall-Tough and conventional austenitic stainless steels. A — Maximum crack length; B — total crack length.

It is also interesting to consider another possible interpretation of the DTA solidification traces, particularly in the case of the Gall-Tough alloy. For the Gall-Tough, the DTA trace returns to the baseline prior to initiation of the secondary on-cooling exotherm, which can be interpreted as the completion of solidification. Therefore, it is conceivable that the Gall-Tough DTA samples solidify entirely as δ-ferrite, and the secondary exotherm represents the solid-state formation of austenite. This view is supported by the

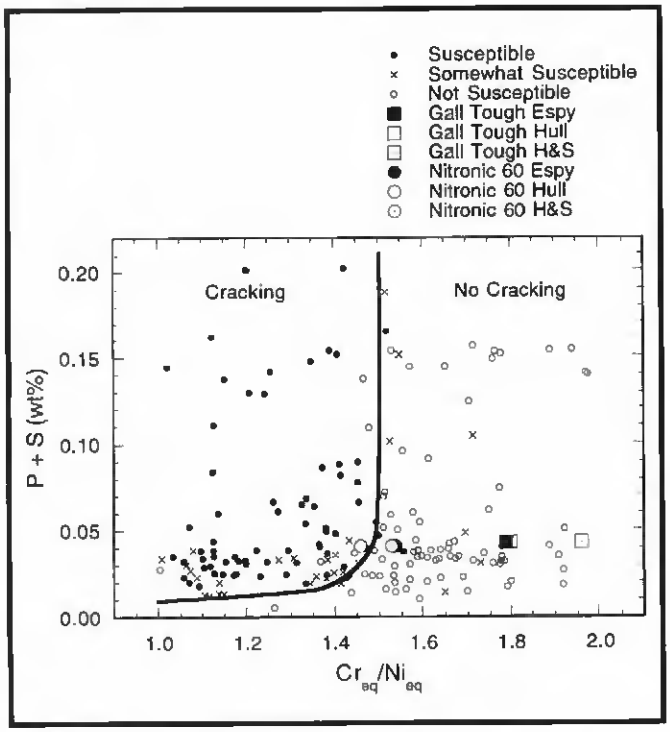

Fig. 8 — Regions of cracking sensitivity as a function of impurity content and Cr_{eq}/Ni_{eq} ratio.

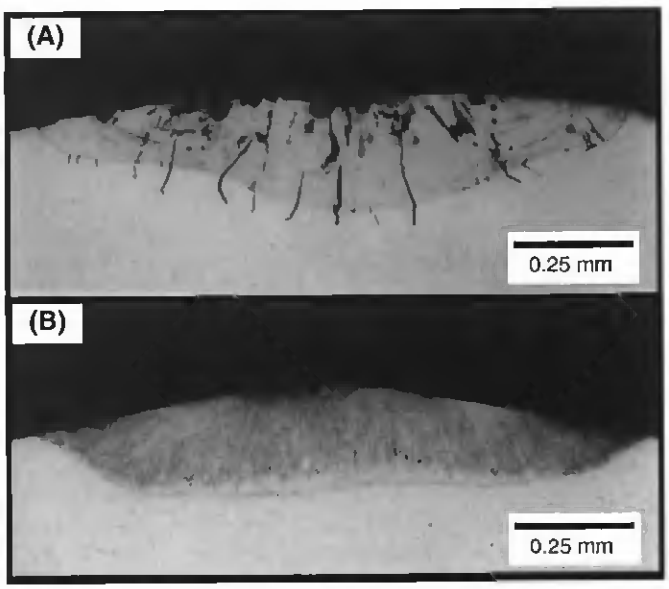

Fig. 9 — Cross sections of laser spot welds. A — Nitronic 60; 8 — Gall-Tough.

relatively high Cr_{eq}/Ni_{eq} ratio of the alloy (Cr_{eq}/Ni_{eq}[Espy] = 1.8) and the observation that the secondary exotherm is small in relation to the primary solidification exotherm (as it should be for a solid-state vs. liquid-solid transformation). In addition, the fraction of ferrite in the Gall-Tough DTA samples (FN ≈ 20) is quite high. Unfortunately, from the microstructural and DTA evidence alone, it is difficult to unequivocally determine whether or not the solidification of Gall-Tough at a cooling rate of 0.33°C/s (0.59°F/s) is single phase or not. However, it is important to note that since the GTA welds in both alloys contained eutectic ferrite and the DTA samples did not, there are some differences between the solidification mechanics of the DTA and GTA weld samples. This implies that cooling rate can have a significant effect on the solidification structure in these alloys, and is discussed further below.

Solidification Hot Cracking

The hot cracking susceptibilities of Nitronic 60 and Gall-Tough, in terms of Varestraint maximum and total crack length, are shown in Fig. 7. By both measures, the heat of Nitronic 60 is somewhat less susceptible to hot cracking than the Gall-Tough. In addition, the minimum augmented strain required for observable cracking is higher in the Nitronic 60 (0.5%) than that for the Gall-Tough (0.75%). Both Nitronic 60 and Gall-Tough are somewhat more susceptible to solidification hot cracking than alloys that are normally considered cracking resistant. As shown in Fig. 7, when compared to 304L and 316 grades with compositions promoting solidification in the ferritic-austenitic mode and tested under the same conditions (Ref. 19), Nitronic 60 and Gall-Tough exhibit maximum crack lengths — roughly two to four times, respectively — than that for the conventional grades at 3% augmented strain. Conversely, compared to alloys that are normally considered hot-cracking susceptible, Nitronic 60 and Gall-Tough exhibit maximum crack lengths — ½ to ¾ times, respectively — than that typical of Alloy 718 at an augmented strain level of 2.5% under similar conditions (Ref. 20). Since the Varestraint testing for the conventional stainless steels and Alloy 718 was conducted using similar test conditions, travel speeds and weld sizes, comparisons between cracking tendencies should be reasonable. Thus, autogenous GTA welds in Nitronic 60 and Gall-Tough can best be characterized as "moderately susceptible to hot cracking." This observation implies that additional precautions, in terms of weld joint restraint and welding procedures, should be taken when autogenously joining these alloys. The results of this work are in general agreement with that of Espy (Ref. 1), who observed that the fabrication and service weldability, using balanced filler metals, of the Nitronic series of alloys was acceptable.

The hot-cracking response, as measured by the Varestraint tests, is qualitatively consistent with the solidification mode and ferrite content diagrams discussed previously. By both these measures of solidification behavior, GTA welds in the two alloys should be reasonably resistant to hot cracking and this is reflected in the Varestraint tests. Unfortunately, there is no currently accepted means for making a direct quantitative comparison between the solidification mode or ferrite content and Varestraint cracking behavior. Taken together, these three measures of hot-cracking response indicate that autogenous GTA processing is feasible, although, as noted above, additional precautions relative to conventional austenitic stainless steels should be considered.

It is well known that the sulfur and phosphorus contents of austenitic stainless steels have a strong influence on weld hot-cracking tendency (Refs. 8, 9). As a result, the general welding response of the Nitronic 60 and Gall-Tough in this context is notable. Figure 8 shows a common means (Refs. 21, 22) of portraying solidification cracking susceptibility in terms of impurity levels and the Cr_{eq}/Ni_{eq} ratio. The Cr_{eq}/Ni_{eq} value of 1.5 corresponds to the change in solidification mode from primary austenite (below 1.5) to primary ferrite (above 1.5). For compositions below 1.5, the boundary between crack-sensitive and crack-susceptible welds is sensitive to the impurity content, while welds above 1.5 remain

crack-resistant even at relatively high impurity levels. Brooks and Thompson (Ref. 9) have reviewed in detail the various rationales that have been proposed to explain the superior hot-cracking resistance of welds that solidify in the primary ferrite mode. As shown in Fig. 8, the heats of Nitronic 60 and Gall-Tough are essentially within the no-cracking region of the diagram. For comparison, several equivalent equations were used for calculating the Cr_{eq}/Ni_{eq} ratios for the alloys and are included in the diagram. These equations include those from Hammer and Svennson (Ref. 23) since these were the equivalents used to construct the diagram. Of the available equivalent formulations, those of Hull (Ref. 17) and Espy (Ref. 1) are shown because they provide the most appropriate descriptions of solidification mode and ferrite content.

No matter which equivalent formulation is used, the Nitronic 60 composition is significantly closer to the boundary for cracking susceptibility; therefore, it is important to consider why the Nitronic 60 performs better in the Varestraint testing. One possibility relates to the impurity content of the alloys (Table 1). Although the combined phosphorus and sulfur levels are similar for the two alloys, the distribution of the two elements is different (*i.e.*, the sulfur level is higher in the Gall-Tough). The diagrams shown in Fig. 8 treat the effects of sulfur and phosphorus with equal weight, which may be an oversimplification. Ogawa (Ref. 24) examined in detail the individual effects of phosphorus and sulfur on the Varestraint hot cracking susceptibility on Invar (a primary austenite solidifying iron-nickel alloy). In that work it was found that sulfur was significantly more potent than phosphorus in promoting cracking. As a result, it was recommended (Ref. 24) that phosphorus and sulfur be kept below 0.010 and 0.002 wt-%, respectively. In the present work, there clearly is insufficient data to distinguish between the individual effects of phosphorus and sulfur, but it is conceivable that the difference in relative levels of these elements contributes to the differences in Varestraint cracking response.

Another important difference between the two alloys is apparent from the DTA results previously discussed. With respect to weld hot cracking, the solidification temperature range is an important quantity (Ref. 25) since it describes the temperature range over which shrinkage strains can develop (and which the remaining liquid must support). Although the DTA experiments do not provide a measure of the equilibrium solidification temperature range, they do provide a means for estimating the solidification temperature range under conditions similar to those encountered in GTAW. Disregarding the effects of fluid flow within the weld pool, a reasonable measure of the solidification temperature range is given by the difference between the on-heating liquidus and the on-cooling solidus from the DTA tests (assuming the DTA tests for both alloys solidify in the ferrite-austenite mode). Using this approach, the solidification temperature ranges for the Nitronic 60 and Gall-Tough are 113 and 144°C (203 and 259°F), respectively. In essence, this temperature range provides a measure of the width of the liquid plus the solid two-phase region that trails the weld pool. Further, the cracks that form in the Varestraint test at high augmented strains are generally considered to be related to the width of this region. The observation that the maximum crack lengths shown in Fig. 7A tend to saturate at an essentially constant value tends to support this interpretation. Thus, it seems likely that the superior cracking response of the Nitronic 60 in the Varestraint test is predominantly a consequence of its smaller solidification temperature range.

Laser Welding Behavior

High-energy-density (HED) welding is often required in the fabrication of miniature components and assemblies and is generally conducted in the autogenous mode. In addition, the rapid solidification velocities and steep thermal gradients associated with HED processing of austenitic stainless steels are known to have dramatic effects on the solidification mode and solidification cracking tendency (see extensive reviews by Brooks and Lippold [Ref. 8] and Brooks and Thompson [Ref. 9]). For these reasons, an evaluation of pulsed laser spot and overlapping welds was conducted. Figure 9 shows the results of laser spot welding trials on the two alloys. As shown, Nitronic 60 exhibits extensive fusion and heat-affected zone (HAZ) cracking, while Gall-Tough does not. These observations were typical of laser spot and seam welds made under a variety of conditions. The results are also consistent with previous work (Ref. 2) on Nitronic 60 in which cracking was observed in laser welds made under a wide range of conditions.

Considering first the fusion zone cracking tendency, it is apparent that under HED processing the Nitronic 60 is generally more susceptible than Gall-Tough to solidification hot cracking. Figure 10 compares the fusion zone microstructures of Nitronic 60 and Gall-Tough. Both alloys were observed to solidify in the primary austenite mode under these conditions. Cracking in the Nitronic 60 (not shown in Fig. 10A) was observed to occur along solidification grain boundaries; however, it should be noted that the dark linear features along the solidification grain boundaries of the Gall-Tough alloy in Fig. 10B are not fine scale cracks. This observation was verified by examining the laser welds in the as-polished condition. Thus, these features appear to be preferentially etched regions along the solidification grain boundaries (possibly ferrite or some minor constituent such as Mn5), which are highlighted by the Nomarski interference contrast imaging mode. Unfortunately, measurement of the ferrite content of the laser welds was precluded by the small size of the welds and by the formation of ferrite in the weld HAZ, as will be discussed below. Based on the etching response, it is assumed that the Nitronic 60 welds contained little or no solidification ferrite, while the Gall-Tough contained a small fraction of eutectic ferrite.

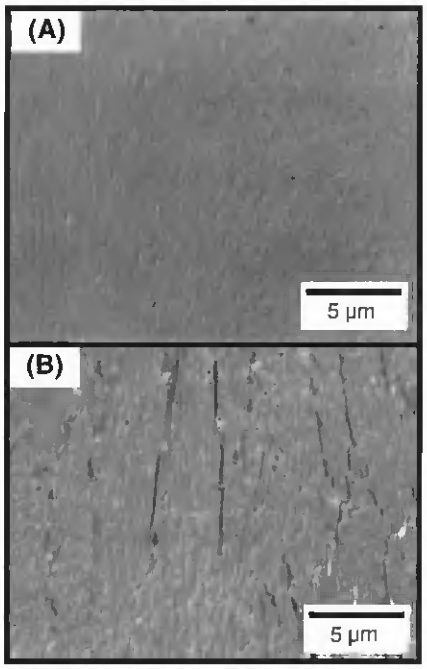

Fig. 10 — Microstructures of fusion zone. A — Nitronic 60; B — Gall-Tough.

As noted above, a change in solidification mode from primary ferrite in GTA welds to primary austenite in HED welds is a common observation. It has been suggested that the change is a result of dendrite tip undercooling (Ref. 9) during the rapid solidification associated with HED processing. Katayama and Matsu-

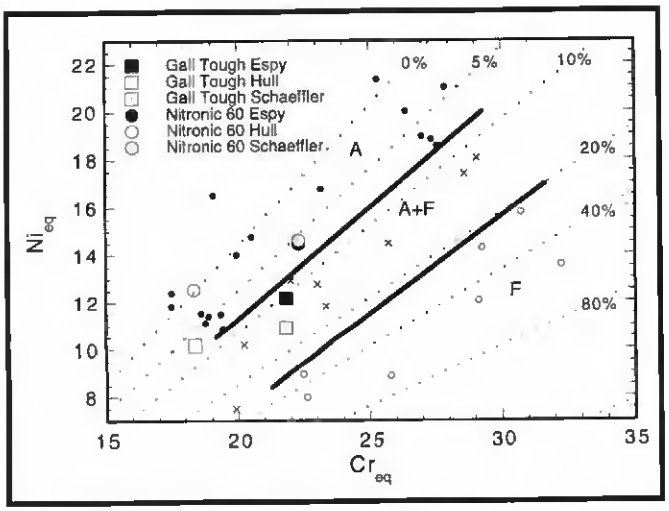

Fig. 11 — HED solidification mode showing location of Nitronic 60 and Gall-Tough compositions.

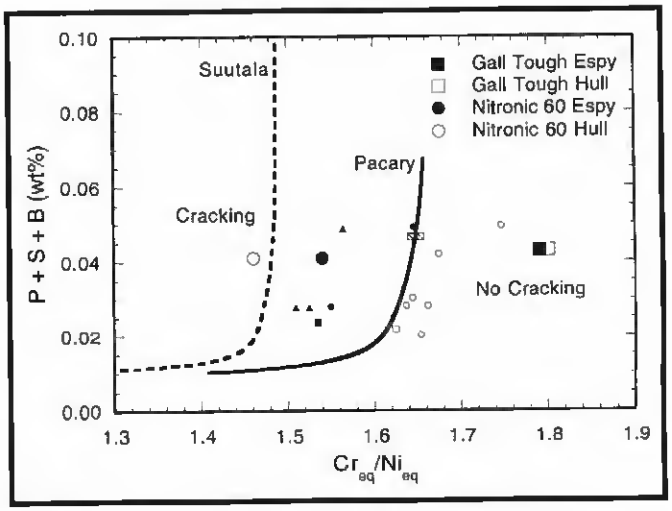

Fig. 12 — Effects of impurity level and composition on solidification cracking susceptibility of pulsed laser welds in austenitic stainless steels.

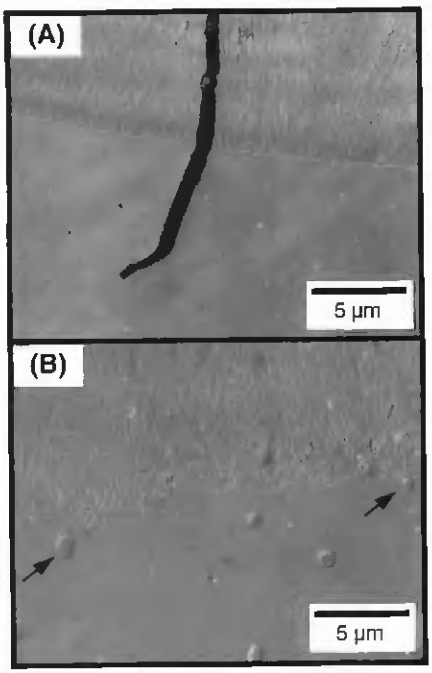

Fig. 13 — Microstructures of laser weld interface region. A — Nitronic 60; B — Gall-Tough (arrows indicate partial liquation of austenite near retained ferrite).

nawa (Ref. 26) constructed a solidification mode diagram for HED welding — Fig. 11. As in Fig. 8, several formulations for the chromium and nickel equivalents for the Nitronic 60 and Gall-Tough are shown in Fig. 11. These equivalents include those due to Schaeffler (Ref. 18) (used to construct the original diagram) as well as the Hull (Ref. 17) and Espy (Ref. 1) equivalents (shown earlier to best describe the behavior of the current alloys). Considering the Espy equivalents to be the most appropriate for the Nitronic 60 and Gall-Tough, it is apparent that the change to primary austenite solidification for both alloys is consistent with the behavior of conventional austenitic stainless steels. The significantly lower Ni_{eq} of the Gall-Tough alloy, however, results in a shift to the primary austenite plus eutectic ferrite mode, while the Nitronic 60 shifts to fully austenitic solidification. From a hot-cracking perspective, the austenitic-ferritic solidification mode (although generally inferior to primary ferrite solidification) is superior to fully austenitic solidification (Refs. 8, 9). Thus, although both alloys shift to a primary austenite solidification mode, the higher Cr_{eq}/Ni_{eq} ratio of the Gall-Tough is sufficient to retain some hot-cracking resistance during HED processing. This point is further illustrated in Fig. 12 (a modification of Fig. 8) to reflect the changes in hot-cracking resistance that accompany HED processing (Refs. 8, 27).

As shown in Fig. 9, cracking in the Nitronic 60 laser welds extends well into the weld HAZ. This cracking is shown in more detail in Fig. 13. The HAZ cracks extend a significant distance into the base metal and are believed to consist primarily of subsolidus cracking, although some liquation cracking near the weld interface is also probable. Evidence for the occurrence of a subsolidus component to the cracking can be obtained by observation of the extent of austenite liquation adjacent to the retained ferrite in the Gall-Tough — Fig. 13B. Apparent liquation of the austenite near the weld interface is apparent within 2–3 μm of the weld interface, while austenite adjacent to ferrite particles further from the weld interface shows no evidence of liquation. Although the DTA results indicate that the liquation temperature for the Nitronic 60 is somewhat lower than the corresponding temperature for the Gall-Tough and it is difficult to observe liquation in the HAZ area of Fig. 13A, it is reasonable to conclude that liquation in the Nitronic 60 does not extend more than approximately 5 μm from the weld interface of the laser welds. Figure 9A shows that HAZ cracks in the Nitronic 60 extend to approximately 50–60 μm from the weld interface; therefore, it is clear that the HAZ cracks must be predominantly subsolidus in character. To more fully characterize the subsolidus cracking response, a series of hot ductility tests were conducted on the two alloys.

Hot Ductility Testing

For Nitronic 60, the range of nil-strength temperatures (NST) at a 100°C/s (180°F/s) heating rate (for three tests) was 1292–1309°C (2358–2388°F) with an average of 1300°C (2372°F). The range for the Gall-Tough alloy was somewhat larger, 1278–1317°C (2332–2403°F), with an average of 1303°C (2377°F). For the Nitronic 60, the NST is reasonably consistent with the DTA results, which indicated initial liquation at 1292°C (2358°F) while in comparison to the DTA measurements for initial liquidation, the NST Gall-Tough measurement was 1327°C (2421°F). Peak temperatures of 1275– 1280°C (2327–2336°F) for Nitronic 60 and 1285–1290°C (2345–2354°F) for Gall-Tough were consequently used to allow for the possibility of a 15°C (27°F) gradient across the

sample thickness for the on-cooling hot ductility tests. A limited number of tests using different peak temperatures were also conducted.

Figure 14 shows the combined results of the hot ductility tests, and it is apparent that there are several differences between the two alloys. The nil-ductility temperature (NDT), or temperature at which the ductility drops to zero on heating, was found to occur at approximately 1261°C (2302°F) for the Nitronic 60. In comparison, the NDT for Gall-Tough was found to occur at approximately 1293°C (2359°F), which is very close to the average measured NST. On cooling from a peak temperature of 1275–1280°C (2327–2336°F), the ductility recovery temperature (DRT) for Nitronic 60 occurs between 910 and 970°C (1670 and 1778°F). For Gall-Tough heated to temperatures in the range 1285–1290°C (2345–2354°F), the DRT is close to 1280°C (2336°F). The traditional interpretation (Ref. 28) of hot-ductility test data is that the cracking sensitivity is related to the extent of nil-ductility in the HAZ and the rate of ductility recovery on cooling. From this, it is generally considered that the magnitude of the temperature range between the NST and DRT is a principal indicator of cracking tendency. By this measure, the cracking sensitivity of Nitronic 60 is significantly higher than that of Gall-Tough.

In HAZ regions more remote from the weld interface, the peak temperatures are much lower than the NST. For these regions, the NDT also provides an important indicator of the relative cracking tendency, since it describes the distance from the weld interface that, at some time during the weld thermal cycle, has essentially no ductility. By this measure, the Gall-Tough is also significantly superior to the Nitronic 60.

Because of the wide range of values encountered in the Gall-Tough NST measurements and the observation that the NST was significantly lower than the initial liquation temperature determined by DTA, several additional tests were conducted to verify the response of the alloy on cooling. For these tests, a higher peak temperature of 1305°C (2381°F) was selected and these results are also shown in Fig. 14. At this higher peak temperature, which is at or above the average measured NST for Gall-Tough, some liquation was apparent. However, the on-cooling ductility response is basically indistinguishable from the DRT obtained from the lower peak temperature tests. Conversely, several on-cooling tests were conducted on the Nitronic 60 using significantly lower peak temperatures of 1263–1266°C (2305–2311°F) and these are also shown in Fig. 14. As with the higher peak temperature tests, little ductility is apparent in the Nitronic 60 at temperatures well below the peak temperature. Unfortunately, insufficient material was available to completely characterize the effect of peak temperature on ductility recovery for either alloy. However, it is clear that the hot-ductility response of the two alloys is markedly different in both on-heating and on-cooling tests. In addition, it seems apparent that these differences are likely to be reflected in the marked difference in laser welding response.

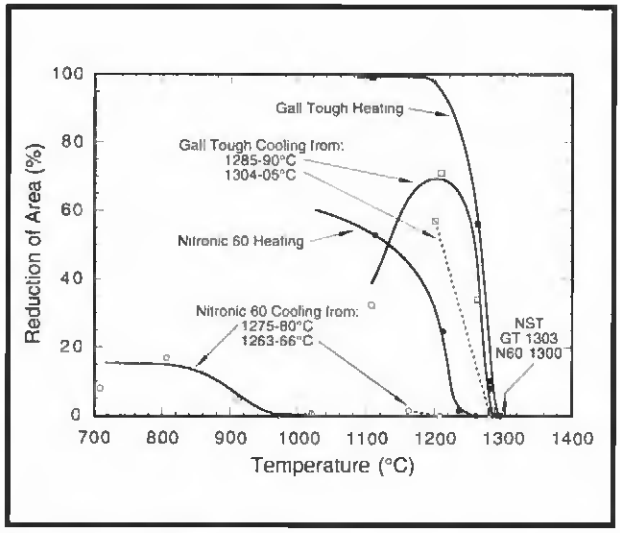

Fig. 14 — Hot-ductility test results for Nitronic 60 and Gall-Tough.

Given the basic similarity in composition between the two alloys, the underlying reasons for the differences in hot-ductility behavior are not readily apparent. Fracture surface analysis indicated that for the peak temperatures used in the majority of the tests — 1275–1280°C (2327–2336°F) for Nitronic 60 and 1285–1290°C (2345–2354°F) for the Gall-Tough — there was generally more incipient melting in the Nitronic 60. This could lead to generally poorer behavior for the Nitronic 60 in the on-cooling tests. The higher fraction of melting does not, however, fully explain the differences observed for the limited testing of Nitronic 60 at lower peak temperatures and Gall-Tough at higher temperatures.

Since the alloys were intended to represent commercial materials, no attempt was made to ensure that the grain size of the alloys was the same. Comparison of the as-received materials indicated that the average grain diameter for the Nitronic 60 was roughly three to four times larger than that for the Gall-Tough. All other factors being equal, finer grain-size materials are generally more resistant to HAZ cracking and, therefore, would be expected to exhibit superior hot ductility. The difference in grain size for the two materials is notable since the annealing temperatures are essentially the same — 1066°C (1951°F) for Nitronic 60 and 1038–1093°C (1900–1999°F) for Gall-Tough. It seems likely that the retained ferrite may restrict grain growth during annealing, so that Gall-Tough may tend to maintain a finer grain size than Nitronic 60. Further, it also seems likely that

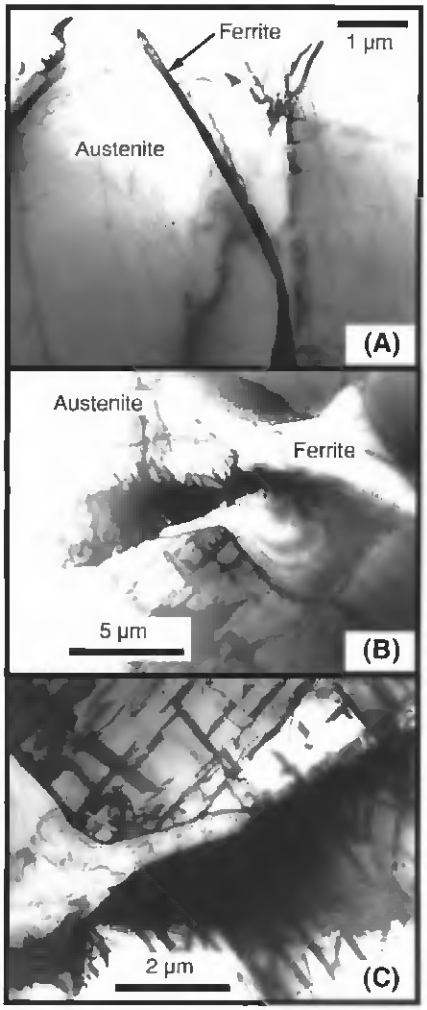

Fig. 15. — TEM micrographs of Gleeble simulation samples. A — Nitronic 60: 1278°C (2332°F) peak temperature, 1020°C (1868°F) test temperature; B and C — Gall-Tough: 1290°C (2354°F) peak temperature, 1284°C (2343°F) test temperature.

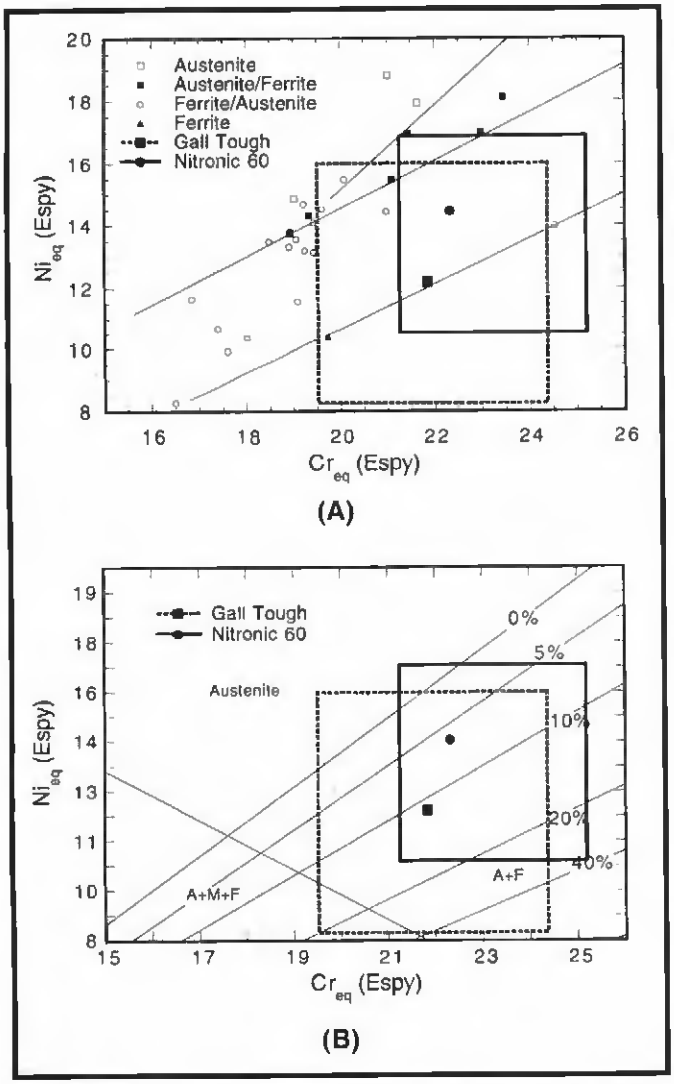

Fig. 16 — Diagram showing composition ranges for Nitronic 60 and Gall-Tough. A — Solidification mode; B — ferrite content.

the retained ferrite in Gall-Tough would tend to restrict grain growth during the hot-ductility testing as well (at least until liquation of the austenite occurs). In turn, this would be expected to improve the relative ductility at high temperatures.

Finally, some initial investigations of the fine-scale microstructures of hot-ductility test samples were conducted. For these evaluations, AEM thin foils were removed from a region adjacent to the fracture surface of zero ductility on-cooling tests. TEM micrographs obtained from these evaluations are shown in Fig. 15. Ferrite (identified by conventional electron diffraction) in the Nitronic 60 HAZ simulations was observed to form thin films along essentially all of the austenite grain boundaries. Conversely, ferrite in the Gall-Tough appears to grow out from the preexisting ferrite and does not generally cover the entire boundary surface. In the case of the Nitronic 60, it is possible that deformation incompatibilities due to strength differences between the austenite and ferrite, or perhaps differences in the segregation of impurity species preferentially to the austenite/ferrite interfaces vs. austenite grain boundaries, may have contributed to the poor high-temperature ductility. Complete characterization of the ferrite morphologies, formation mechanism and deformation response would require metallographic examination of samples treated to a wide range of peak temperatures and cooling conditions. Such an evaluation was, unfortunately, outside the scope of this study. Nevertheless, it seems apparent that the relative hot ductility of the two alloys is dominated by differences in the way ferrite evolves at high temperatures. Further, it is also apparent that the transformation to ferrite in the HAZ is strongly dependent on the details of the thermal cycle and, thus, the welding procedures.

Additional Observations

There are several additional observations with respect to autogenous welding of these alloys that should be noted. First, the Varestraint test apparatus used in this work is equipped with a fully enclosed welding area that has been successfully used for Varestraint testing of titanium alloys. Despite this very clean environment, both alloys tend to form a tenacious surface scale (containing manganese, silicon and oxygen) that can affect bead control during welding. A similar scale was formed on the surface of the laser spot welds and can be seen in the micrograph of Fig. 9A. The formation of the surface scale results in a net depletion of Mn and Si in the weld metal, but the level of this depletion was not quantified. Clearly, the depletion is likely to be dependent on welding conditions and can affect the solidification characteristics of the welds.

More importantly, however, metallographic examination of the GTA welds showed that a region of dense intergranular precipitation formed in both alloys in a region 1–2 mm from the weld interface. Clearly, this precipitation is characteristic of a sensitized region that may have reduced corrosion resistance. Presumably, a postweld heat treatment (PWHT) similar to that used for other sensitization-prone austenitic stainless steels would probably be effective in mitigating this problem.

Finally, it is important to reiterate that the current study was conducted on a small number of heats. Figure 16 shows the solidification mode and ferrite diagrams of Fig. 4 with the composition ranges for each alloy superimposed on the diagram. From the size of these ranges, it is apparent that, like other austenitic stainless-steel grades, a wide range of response is possible within a specific alloy designation. However, given the fact that specialty alloys are not generally produced at the extremes of their composition ranges and specific composition and microstructural differences between the two alloys exist it is assumed that the results of the present study are generally applicable.

Summary and Conclusions

The solidification and welding behavior of Nitronic 60 and Gall-Tough have been evaluated by differential thermal analysis, Varestraint testing, hot-ductility testing and microstructural analysis. The results of this work can be summarized as follows: Autogenous GTA welds in both alloys solidified by the ferritic-austenitic mode, although the higher Cr_{eq}/Ni_{eq} ratio of Gall-Tough resulted in a higher fraction of ferrite in the welds. The solidification mode and ferrite fraction of both alloys was best described using chromium and nickel equivalents developed specifically for the Nitronic series of alloys. Both alloys were found to be somewhat more susceptible to solidification hot cracking than conventional austenitic stainless steels, but autogenous GTA processing of the alloys is feasible. For GTA welds, the Varestraint hot-cracking resistance of Nitronic 60 was superior to Gall-Tough, apparently because of the larger solidification temperature range of the Gall-Tough. Laser

spot welding trials resulted in both fusion and HAZ cracking in the Nitronic 60, while Gall-Tough was generally resistant to fusion zone and HAZ cracking in these high-solidification-rate, high-restraint welds. Comparison of the laser weld microstructures indicated that Nitronic 60 shifts to fully austenitic solidification, while the higher Cr_{eq}/Ni_{eq} ratio of Gall-Tough tends to limit the shift in solidification mode to an austenitic-ferritic solidification mode in HED processing. Hot-ductility measurements indicated that Gall-Tough is generally superior to Nitronic 60 in both on-heating and on-cooling tests and has a very small nil-ductility region. The superior hot ductility of Gall-Tough apparently results from differences in grain size between the heats tested, as well as differences in the mechanism of ferrite formation at high temperatures.

Acknowledgments

The authors would like to express their thanks to the staff at Sandia National Laboratories who contributed to this work: Fred Greulich and Alice Kilgo for optical metallography, Paul Hlava and Dick Grant for EPMA analysis, Bonnie McKenzie for SEM analysis, Tom Chavez for preparation of the AEM thin foils and, finally, special thanks to Mike Cieslak for his valuable comments and thoughtful review of the manuscript. Sandia is a multiprogram laboratory, supported by the U.S. Department of Energy under Contract DE-AC04-94AL85000.

References

1. Espy, R. H. 1982. Weldability of nitrogen-strengthened stainless steels. *Welding Journal* 61(5): 149-s to 156-s.

2. Maguire, M. C., Robino, C. V., Damkroger, B. K., and Lienert, T. J. 1993. Heat-affected zone cracking of Nitronic 60 stainless steel. 74th Annual American Welding Society Exposition and Convention, Miami, Fla., pp. 116–117.

3. Brooks, J. A. 1975. Weldability of high N, high Mn austenitic stainless steel. *Welding Journal* 54(6): 189-s to 195-s.

4. Bennett, W. S., and Mills, G. S. 1974. GTA weldability studies on high manganese stainless steel. *Welding Journal* 53(12): 548-s to 553-s.

5. Suutala, N. 1982. Effect of manganese and nitrogen on the solidification mode in austenitic stainless steel welds. *Metallurgical Transactions* 13A: 2121–2130.

6. Ritter, A. M., and Savage, W. F. 1986. Solidification and solidification cracking in nitrogen-strengthened austenitic stainless steels. *Metallurgical Transactions* 17A: 727–737.

7. Ritter, A. M., Henry, M. F., and Savage, W. F. 1984. High temperature phase chemistries and solidification mode prediction in nitrogen-strengthened austenitic stainless steels. *Metallurgical Transactions* 15A: 1339–1351.

8. Brooks, J. A., and Lippold, J. C. 1993. Selection of wrought austenitic stainless steels. *ASM Metals Handbook* 6: 456–470.

9. Brooks, J. A., and Thompson, A. W. 1991. Microstructural development and solidification cracking susceptibility of austenitic stainless steel welds. *International Metals Reviews* 36: 16–44.

10. Cieslak, M. J., Headley, T. J., Kollie, T., and Romig, Jr.,A. D. 1988. A melting and solidification study of Alloy 625. *Metallurgical Transactions A* 19A: 2319–2331.

11. MacIssac, D., Shiohara, B. Y., Chu, M. G., and Flemings, M. C. 1983. Structure of undercooled iron and nickel-based alloys. *Grain Refinement in Casting and Welds*, eds. G. J. Abhaschian and S. A. David. TMS, pp. 87–96.

12. Savage, W. F., and Lundin, C. D. 1965. The Varestraint test. *Welding Journal* 44(10): 433-s to 442-s.

13. Goehner, R. P., and Michael, J. R. 1996. Phase identification in a scanning electron microscope using backscattered electron kikuchi patterns. *Journal of Research of the National Institute of Standards and Technology* 101: 301–308.

14. Scott, V. D., and Love, G. 1983. *Quantitative Electron-Probe Microanalysis*. John Wiley, New York, pp. 218–232.

15. Suutala, N., Takalo, T., and Moisio, T. 1980. Ferritic-austenitic solidification mode in austenitic stainless steel welds. *Metallurgical Transactions* 11A: 717–725.

16. Cieslak, M. J., Ritter, A. M., and Savage, W. F. 1982. Solidification cracking and analytical electron microscopy of austenitic stainless steel weld metals. *Welding Journal* 61(1): 1-s to 8-s.

17. Hull, F. C. 1973. Delta ferrite and martensite formation in stainless steels. *Welding Journal* 52(5): 193-s to 203-s.

18. Schaeffler, A. L. 1949. Constitution diagram for stainless steel weld metal. *Metals Progress* 56: 680 and 680B.

19. Robino, C. V., Hills, C. R., and Hlava, P. F. 1994. Characterization of solidification and weldability of Fe-29Ni-17Co alloys. *Low Thermal Expansion Alloys and Composites*, eds. J. J. Stephens and D. R. Frear. The Metals Society of AIME, Warrendale, Penn., pp. 123–138.

20. Robino, C. V., Michael, J. R., and Cieslak, M. J. 1997. Solidification and welding metallurgy of thermo-span alloy. *Science and Technology of Welding and Joining* 2: 220–230.

21. Kujanpaa, V., Suutala, N., Takalo, T., and Moisio, T. 1979. Correlation between solidification cracking and microstructure in austenitic and austenitic-ferritic stainless steel welds. *Welding Research International* 9: 55–76.

22. Takalo, T., Suutala, N., and Moisio, T. 1979. Austenitic solidification mode in austenitic stainless steel welds. *Metallurgical Transactions A* 10A: 1173–1181.

23. Hammar, O., and Svennson, U. 1979. Influence of steel composition on segregation and microstructure during solidification of austenitic stainless steels. *Solidification and Casting of Metals* The Metals Society, London, pp. 401–410.

24. Ogawa, T. 1986. Weldability of Invar and its large-diameter pipe. *Welding Journal* 65(8): 213-s to 226-s.

25. Borland, J. C. 1960. Generalized theory of super-solidus cracking in welds (and castings). *British Welding Journal* 7(8): 508–512.

26. Katayama, S., and Matsunawa, A. 1985. Solidification behavior and microstructural characteristics of pulsed and continuous laser welded stainless steels. *Proceedings of the International Conference on Applications of Lasers and Electo-Optics.***** San Francisco, Calif., pp. 19–25.

27. Lippold, J. C. 1994. Solidification behavior and cracking susceptibility of pulsed-laser welds in austenitic stainless steels. *Welding Journal* 73(6): 129-s to 139-s.

28. Duvall, D. S., and Owczarski, W. A. 1967. Further heat-affected-zone studies in heat resistant nickel alloys. *Welding Journal* 46(8): 423-s to 432-2.